Supplementary Figures

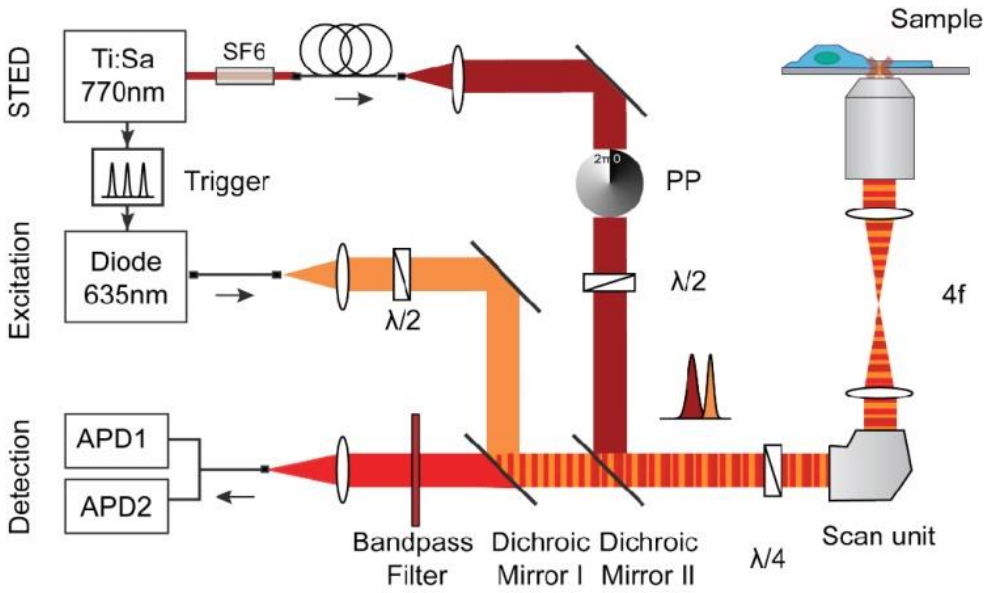

Supplementary Figure 1. sSTED-FCS setup with pulsed excitation (orange) and STED (red) lasers and according beam paths. The repetition rates of the two lasers were synchronized using an electronic trigger box. The laser beams were overlaid using two dichroic mirrors and focused into the sample. The emitted fluorescence (red) was cleaned using a bandpass filter and detected using two fiber-coupled avalanche photon detectors (APD). The fluorescence was imaged onto the input of a 50:50 splitting fiber, serving as the confocal pinhole. The polymeric phase plate (PP) induced a clockwise 2π-phase shift across the STED beam which generated the doughnut shaped intensity distribution in the focal plane. Note, that the circular polarization of both laser beams is maintained by a combination of $\lambda/2$ and $\lambda/4$ waveplates. The STED laser was further sent through SF6 glass rods (SF6) and a 120m-long polarization maintaining single-mode fiber (PMS) for stretching of the pulses and mode cleaning.

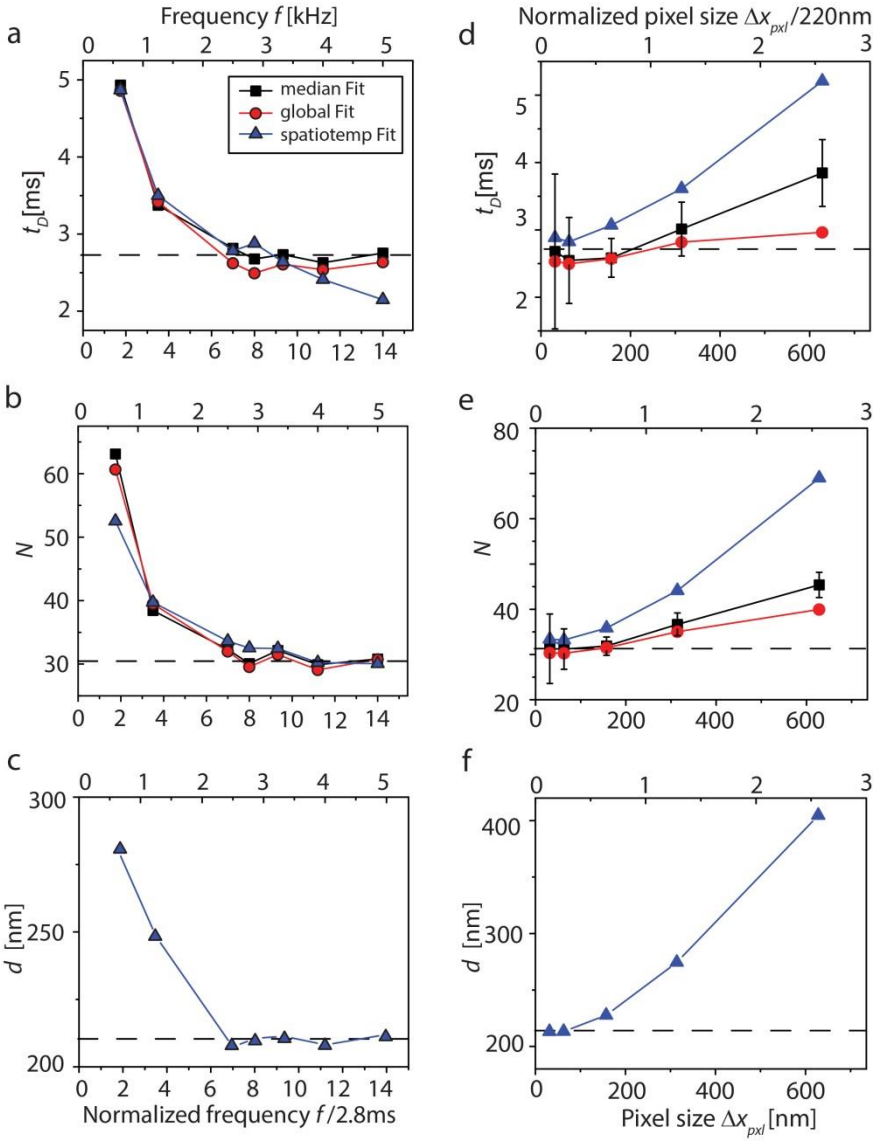

Supplementary Figure 2. Evaluation of optimal scan parameters from analysing scanning FCS data. The average transit time t_D (**a,d**), particle number N (**b,e**) and diameter d of the observation spot (**c,f**) are shown as a function of scanning frequency f and pixilation Δx_{pxl} of the orbital scan (average of 10 data points; error bars = standard deviation of the mean, s.d.m.). The parameters were determined from temporal (a,b,d,e) and spatial correlations (c,f) of confocal scanning FCS data of a fluorescent phosphoethanolamine analog (PE-KK114) diffusing in a phospholipid (DOPC) membrane bilayer spin-coated on plasma-cleaned cover glass (DOPC:PE-KK114 1:0.01, R = 2µm, Δx_{pxl} = 50 nm (a-c), f =3.3 kHz (d-f)). The dashed line (t_D = 2.8 ms, N = 30, d = 220 nm) reveals the values obtained from single-spot measurements, indicating optimum parameters of $f > 4/t_d$ and $\Delta x_{pxl} < 3\ d$ for scanning (STED-)FCS. Results of the temporal correlations are shown for different analyses (median fit (black): fit of equation (1) to the temporal correlation curve generated as the median of all correlation curves, global fit (red): fits of equation (1) to each temporal correlation curve of the orbital scan with global values of t_D and N, spatiotemporal fit: values extracted from fitting equation (2) to the spatiotemporal correlation curve generated as the median of all correlation curves) and plotted against the real values of f (upper axes) and Δx_{pxl} (lower axes) as well as against their normalized values f/2.8 ms (lower axes, with t_D = 2.8 ms being the correct average transit time through the d = 220 nm large confocal observation spot) and Δx_{pxl}/220 nm (upper axes, with d = 220 nm being the diameter of the confocal observation s), respectively.

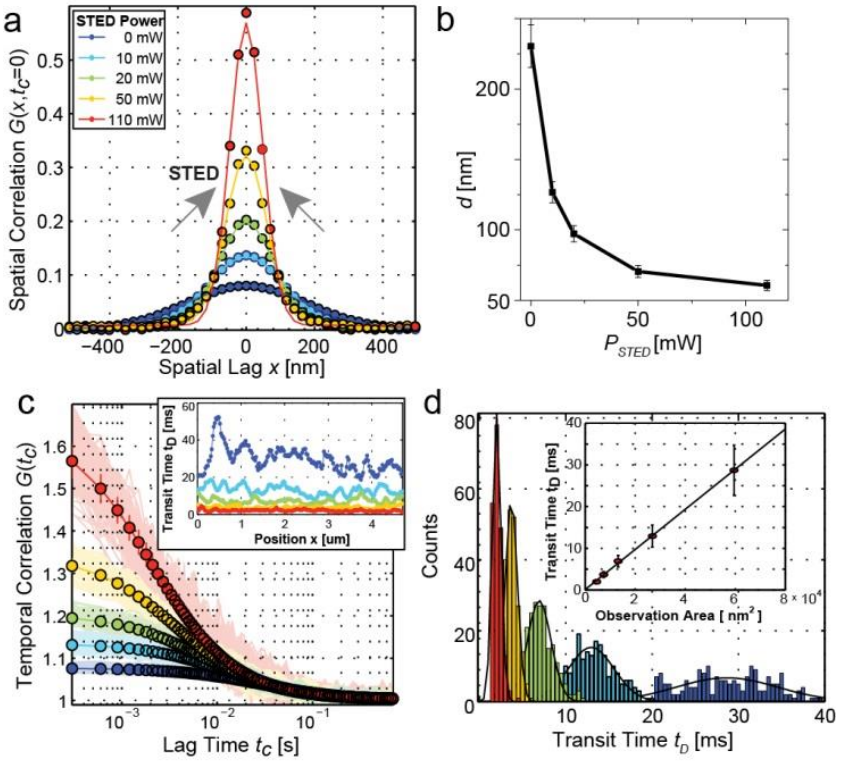

Supplementary Figure 3. sSTED-FCS on supported DOPC model membranes investigating the mobility of fluorescently labeled CtxB bound to the ganglioside lipid GM1. (**a**) Spatial correlation function $G(x,t_c=0)$ along the intensity curtain generated from the sSTED-FCS measurement on CtxB-GM1 for different STED powers P_{STED} as given in the inset. The narrowing of $G(x,t_c=0)$ for increasing P_{STED} reveals the confinement of the observation spot (arrows) (average of 10 measurements). (**b**) Dependence of the diameter d of the observation spot on the STED-laser power P_{STED} as determined from fitting equation (3) to the data of (a). (**c**) Temporal correlation $G(t_c)$ of the intensity carpet resulted in 200 individual FCS curves for each P_{STED}, whose averages are plotted (color code as in a, individual curves are shown in sallow) revealing an increase of the amplitude and a decrease of the decay time with P_{STED}. (Inset) The spatial dependence of the transit time t_D is highlighted by plotting values of t_D along the orbital scan path x, as determined from analyzing the individual FCS curves of the orbital scan using equation (1). (**d**) The distribution of transit times t_D from the scans of b with different P_{STED} (color code as in (a) and (c)) can be described by a Gaussian (solid lines) to obtain the mean transit times and their relative standard deviations. (Inset) Consequently, from a single series of sSTED-FCS measurements only, one can determine the dependency of the mean transit time t_D on the size of the observation area ($\pi(d/2)^2$) with a large body of data for analysis (average over 200 data points), whose linear relationship (solid line) reveals dominantly free Brownian diffusion. Error bars = s.d.m.

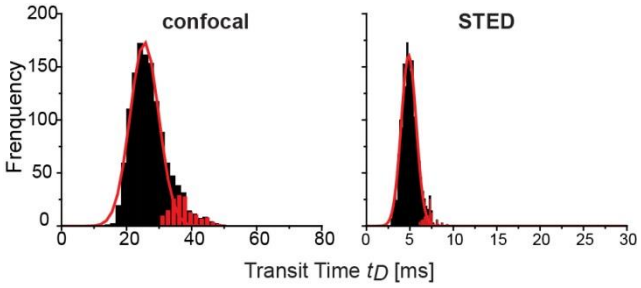

Supplementary Figure 4. Histograms of the transit times t_D of the simulated data of free diffusion of Fig. 1c for confocal (250 nm, left) and STED (80 nm, right) recordings (1500 data points for confocal and STED, respectively). Histograms are built up as in Fig. 4a. The main peak of the histogram (black) was fitted with a single Gaussian (red line) and the residuals classified as tail (red). In comparison to the PE and SM data (Fig. 2a) the fraction of the events in the tail are much lower and the data was better described by a single Gaussian fit.

a

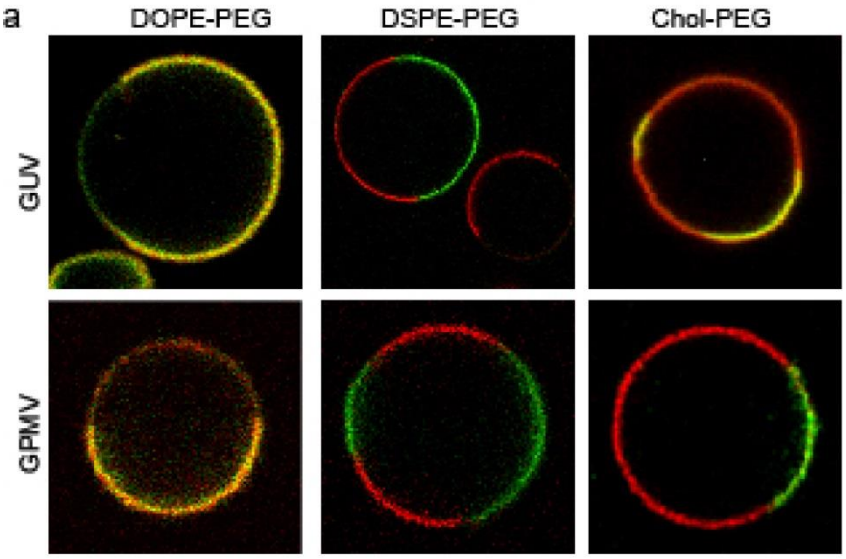

b

Probe	GUV *Lo%*	GPMV *Lo%*
PE	5 ± 1	16 ± 1
SM	3 ± 1	18 ± 5
DOPE-PEG	12 ± 2	30 ± 2
DSPE-PEG	70 ± 3	80 ± 3
Chol-PEG	50 ± 2	60 ± 2

Supplementary Figure 5. Partitioning of the different fluorescent lipid analogues in phase-separated giant-unilamellar-vesicles (GUVs) and giant-plasma-membrane-vesicles (GPMVs, generated from PtK2 cells). (**a**) Representative scanning confocal images of phase-separated GUVs (upper panels) and GPMVs (lower panels) for DOPE-PEG (left), DSPE-PEG (middle) and Chol-PEG (right). The fluorescence intensity detected for the PEG-lipid analogs is given in red, and that of the fluorescent fast-DIO lipid in green. The latter marks less ordered (liquid-disordered, Ld) areas of the membrane. Yellowish regions mark regions of roughly equal amount of fluorescence signal from PEG-lipid analogues and fast-DIO. The occurrence of red regions consequently indicates a strong partitioning of the respective lipid analog into more ordered (liquid-ordered, Lo) areas of the membrane. (**b**) Table listing the liquid-ordered partitioning coefficients %*Lo* of the different fluorescent lipid analogs in GUVs and GPMVs. Values of %*Lo* were determined from scanning images (as in (a)) of 10-15 vesicles, as described in Supplementary Note, and indicate what molecular fraction of the analogs partitions into the more liquid-ordered (Lo) membrane regions (errors = s.d.m.). Large values reveal a preference of the respective fluorescent lipid analog for more ordered membrane areas. Clearly, DSPE-PEG and Chol-PEG prefer more ordered regions, while all others prefer less ordered regions.

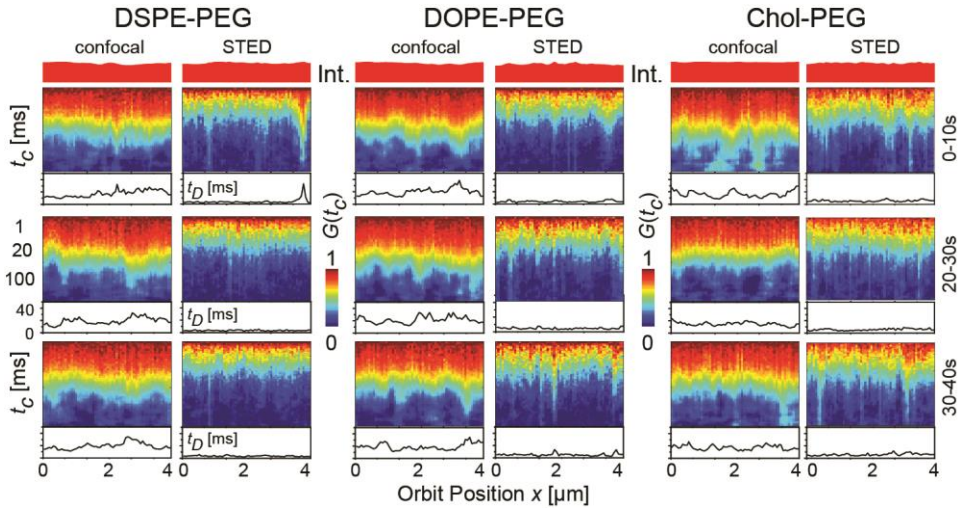

Supplementary Figure 6. Time-dependent confocal and STED correlation carpets of the pegylated fluorescent lipid analogs. Direct comparison of confocal and STED scanning recordings of DSPE-PEG (left), DOPE-PEG (middle) and Chol-PEG (right): Total intensity (upper panels, normalized), correlation carpets (middle panels) and transit times t_D (lower panels) diffusion for confocal and STED recordings for measurements at 10-s consecutive time windows, as labelled on the right. The correlation carpets are presented as in Figs. 5 and 6.

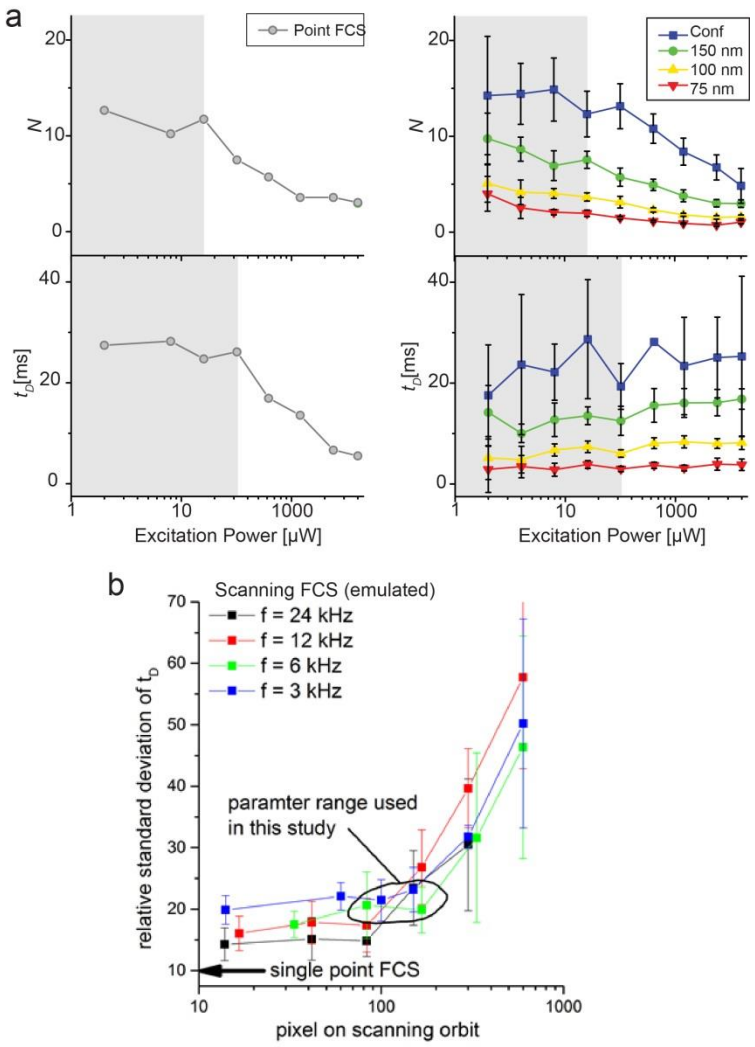

Supplementary Figure 7. (**a**) Reduced photobleaching in sSTED-FCS measurements. Particle number N (upper panels) and average transit time t_D (lower panels) as a function of excitation power. 12 correlation curves were recorded for confocal single-point FCS (left column) and sSTED-FCS measurements (right column) on the fluorescent cholera-toxin B-GM1 complex diffusing in a phospholipid (DOPC) membrane bilayer spin-coated on plasma-cleaned cover glass (DOPC:GM1 1:0.01, R = 2 µm, Δx_{pxl} = 50 nm, f =3.3 kHz). A reduction of N and t_d indicates photobleaching of the fluorescent label before leaving the observation spot, which was significantly reduced for the scanned recordings, allowing the institution of larger excitation powers. Error bars = s.d.m.

(**b**) Error estimation of sSTED-FCS compared to single point FCS. Ten 100s single point measurements of PE-KK114 diffusing in a DOPC SLB were recorded in form of a photon trace (detected photons with time of arrival within measurement) with full time resolution (80 MHz). The photon trace was subdivided into 10-s traces, correlation data calculated as described in the Methods section, and the average transit times determined by fitting equation (1) to the data. The relative standard deviation (in % of the absolute value) was 10% for the single point measurement. Scanning the observation spot introduces two effects on the sampling of the photon trace. First the sampling rate is reduced by spitting the scanning trajectory into n pixels and secondly the time resolution is decreased to the limited scanning frequency f. To estimate the additional error introduced by scanning the same photon traces from the single point measurement were used to emulate scanning. First photons were discarded according to the number of pixels on the trajectory and then the photon trace was binned according to the scanning frequency. As expected the results show that the relative standard deviation for each correlation curve on the scanning trajectory increased when the trajectory was subdivided into more pixels. Additionally, the plot shows that there were two regimes which determined the precision of the FCS measurement in scanning FCS. At high number of pixels (> 100) the standard deviation was independent of the scanning frequency, while at a lower number of pixels an increase of the scanning frequency improved the precision of the measurement approaching the value for single-point FCS measurements. For the applied scanning parameters in this work the relative standard deviation was 2.5-times higher in each pixel of the scanning orbit. However, if the spatial information was omitted and all pixels from the whole scanning trajectory were pooled the relative standard deviation was 5-times increased.

Supplementary Table 1.

Determination of number, positions, average width, and average distance of trapping sites of the three correlation carpets of SM of Fig. 5, indicating that these sites appear and disappear from one 10-s recording to the next.

Carpet	Number	Positions	Width	Distance
0-10s	7	2, 10, 21,32,46,56,63	5.5	10
10-20s	10	1, 8, 11, 20, 25,34, 42, 49, 56, 63	5	7
20-30s	8	8, 19, 27, 36, 45, 49, 54, 62	5.5	7

Sites were detected as long decays (peaks) in the correlation carpet with a threshold at 15 ms correlation time.
The different parameters are given in units of pixels (pixel width 15 nm):

- Positions: pixel positions of the peaks in the orbital scan.
- Width: average FWHM of the peaks.
- Distance: average peak-to-peak distance.

Supplementary Notes

Supplementary Note 1 - Optimization of scanning parameters

Scanning-FCS data recorded for the fluorescent phospholipid analog PE-KK114 diffusing in a supported lipid-membrane (DOPC) (Supplementary Fig. 2) showed that diffusion parameters such as the average transit time t_D = 2.8 ms through the confocal observation spot were most accurately determined from the correlation data for f > 3 kHz, i.e. with a time base of the recorded fluctuation data of $\Delta T = 1/f$ < 0.3 ms. For general values of t_D, we could confirm that frequencies $f > 4/t_D$, i.e. $\Delta T < t_D/4$ were required to accurately reproduce the diffusion properties of the sample. Using the same set of experiments, we determined that the minimal pixilation (pixel width) Δx_{pxl} of the scan orbit had to be three times smaller than the diameter the observation spot (i.e. $\Delta x_{pxl} < 3\ d$).

Supplementary Note 2 - sSTED-FCS on supported lipid bilayers

We next exemplified the performance of our sSTED-FCS experiments using a supported lipid membrane (SLB) as a defined model system for two-dimensional (2D) membrane diffusion. This SLB was prepared from unsaturated phospholipids (DOPC) on cleaned glass cover slides, and contained 0.1 mol % of the ganglioside GM1 which we labeled with fluorescent cholera toxin B (CtxB) tagged with the red-emitting dye KK114[1]. The labeling degree of CtxB was < 2. The mobility of GM1 was measured using sSTED-FCS with total recording times between 12 s and 24 s. We chose the GM1-CtxB complex for our proof-of-principle studies, since binding of CtxB to GM1 ensured slow-down of the ganglioside lipid's mobility, and the temporal resolution of the sSTED-FCS data was thus good enough to accurately capture the diffusion parameters. On the other hand, the concentration of both GM1 and CtxB was low enough to ensure prominently free Brownian diffusion, albeit we observed significant hindrances in diffusion at larger concentrations[2].

Spatial correlation: Determination of the observation spot diameter

We first exemplify how sSTED-FCS allowed us to determine the diameters d of the observation spots for different powers P_{STED} of the pulsed STED laser directly from the individual data by spatially correlating the pixels along the orbit[3-5]. The central peak of the spatial correlation function $G(x,t_c=0)$

(with pixel position x and correlation time t_c) decays according to the size of the observation spots. Choosing a large enough scanning velocity, this decay is independent of the diffusion, as outlined in equation (3). Following the spatial correlation analysis, the diameter d of the observation spot measured as the full-width-at-half maximum (FWHM) value decreased with increasing STED power P_{STED} at the sample (Supplementary Fig. 3a), namely from d = 250 nm without STED to d = 60 nm for P_{STED} = 110 mW (Supplementary Fig. 3b). This decrease was in line with independent calibrations of the FWHM using single-point FCS measurements as well as imaging 20 nm sized fluorescent beads[6,7].

Temporal correlation: Capturing diffusion parameters simultaneously at different points in space

Supplementary Figure 3c depicts the temporal correlation data $G(t_c)$ (with correlation time t_c) for varying P_{STED}. An increase in amplitude and a decrease in decay time became obvious for increasing P_{STED}. While the amplitude is inversely proportional to the average particle number N in the observation spot, the decay scales with the average transit time t_D through the observation area. Fitting the data confirmed that both parameters decreased with increasing P_{STED}, i.e. with decreasing size of observation spot [7]. Most importantly, using the scanning approach, we could now determine the average transit time t_D along the positions of the orbit and potentially detect diffusion heterogeneities in space (inset Supplementary Fig. 3c). Such heterogeneities should become directly apparent as local peaks when plotting t_D along the scanned pixels. Note that to gain statistical significance about heterogeneities in space, multiple scanning orbits have to be analyzed (see for example histogram analysis in Fig. 2 and Supplementary fig. 7), as outlined in the next section.

Temporal correlation: Capturing diffusion parameters with a large body of data for analysis

A statistically precise allocation of heterogeneity is derived from the large number of t_D values collected over all pixels of a single sSTED-FCS measurement. A histogram of all t_D values allowed a precise determination of average values and a straightforward disclosure of any deviation from a normal (i.e. Gaussian) distribution. Supplementary Fig. 3d depicts these histograms for the CtxB mobility on the DOPC SLB membrane. All histograms obtained for the different P_{STED} could be well described by a single Gaussian distribution with the same relative width (sigma) of ~20%, indicating

Brownian free diffusion. Note that the largest absolute numbers of standard deviations in values of t_D are of course obtained for the Gaussian distributions around large values of t_D, i.e. for the confocal measurements. Nevertheless, the relative standard deviations (in % of the average value of t_D) are comparable for all histograms, meaning that the heterogeneity is comparable for all measurements. Free diffusion was also found when plotting the average values of t_D against the area of the observation spot (inset Supplementary Fig. 3d). This dependence was linear with an intercept at the origin (as expected for free Brownian diffusion[8]), revealing an average lateral diffusion coefficient of $D = 0.14 \pm 0.01\ \mu m^2\ s^{-1}$.

sSTED-FCS: General advantages and limitations

From the above experiments we concluded that sSTED-FCS has several advantages over single-point STED-FCS. 1) A large number of values for parameters such as the transit time can be collected during a single sSTED-FCS recording (Fig. 2). This aspect allows the determination of their average and a more straightforward disclosure of heterogeneous diffusion modes from a single sSTED-FCS measurement. In single-point STED-FCS experiments, a multitude of measurements are required to reach the same large body of data for analysis. 2) Spatial variations in diffusion characteristics and heterogeneous diffusion environments can be detected just by plotting the transit times as a function of the spatial positions (Fig. 3). 3) In sSTED-FCS the observation spot diameter can be determined from the measurement itself using spatial correlation analysis (Supplementary Fig. 3). In contrast, in stationary single-point STED-FCS the observation spot size cannot be determined directly; additional calibration measurements are required[6]. 4) As has been demonstrated before for conventional scanning FCS[4,9,10] bias due to photo bleaching was reduced (Supplementary Fig. 7a). This reduction enables the study of relatively slow diffusion processes such as the mobility of proteins in the plasma membrane, without having to reduce the excitation power and thus the brightness of the detected signal.

Compared to conventional scanning FCS, a main constraint of sSTED-FCS is its temporal resolution [4,9,10]. The fastest diffusion processes that can be studied are limited by the maximum applicable

scanning frequency, in our case 4 kHz, meaning that molecules should have a transit time through the observation spot of > 0.8 ms. For standard confocal recordings this transit time amounts to a diffusion coefficient of $D \approx 10\ \mu m^2\ s^{-1}$ or lower, which is much faster than the diffusion processes studies here. In addition, compared to single-point measurements the scanning process lowers the sampling rate of an individual correlation curve, thus reducing the signal-to-noise ratio of a single correlation curve in one pixel of the scan (Supplementary Fig. 7b). This becomes even more pronounced for STED recordings, since with its reduced observation spots the transit time and often also the signal-to-noise ratio decrease[7]. However, if the spatial information was omitted and all pixels from the whole scanning trajectory were pooled (as in Fig. 3c), the statistical accuracy of a sSTED-FCS recording would be 5-times higher than that of a non-scanned single-point FCS measurement (Supplementary Fig. 7a).

Supplementary Note 3 – Further explanation of Figure 7

For each correlation curve (pixel) of the sSTED-FCS recordings values of the transit time t_D and average particle number N were determined by fitting equation (1) to the FCS data. While the transit time reports on the local mobility of the fluorescent lipid analogs, the average particle number is a measure of their local concentration (see equation (1) for definitions). Normalized values $t_D / \langle t_D \rangle$ and $N/\langle N \rangle$ were calculated by division with the respective average values $\langle t_D \rangle$ and $\langle N \rangle$ determined over all pixels of each scan trajectory. Two dimensional frequency histograms of pixel value pairs of $t_D / \langle t_D \rangle$ and $N/\langle N \rangle$ were then generated in MATLAB and plotted as two-dimensional contour plots with the color code indicating frequency of occurrence of a specific value pair.

We expect the following characteristic two-dimensional histograms or correlation plots $t_D / \langle t_D \rangle$ vs. $N/\langle N \rangle$, which might depend on the phase partitioning characteristics of the investigated fluorescent lipid probe:

- In the absence of heterogeneity no correlation is expected for any probe, since they will be homogeneously distributed, i.e. the local concentration is constant over space with a distribution around $N/\langle N \rangle = 1$ given by experimental standard deviations. For freely

diffusing probes, we expect an isotropic distribution around the origin (t_D /<t_D>; N/<N>) = (1;1), since also the transit times are homogeneous (compare Supplementary Figure 4). In contrast, for trapped diffusion (i.e. transient arrests due to interactions with slow-moving or immobilized molecules as for SM) we expect a tail towards large t_D (compare Fig. 4).

- In case of distinct Lo domains within a Ld membrane ("lipid rafts") and a Lo-partitioning lipid probe we expect a positive correlation (right tilt), since due to its partitioning behavior the probe will accumulate in the Lo domains, where mobility is reduced.
- Under the same conditions we expect a negative correlation (left tilt) for a liquid-disordered (Ld)-preferring lipid probe , since the probe will avoid areas of reduced mobility (the Lo domains) and accumulate in the remaining Ld regions of increased mobility.
- A positive correlation (right tilt) is expected for locally curved membrane regions independent of the phase preference of the lipid probe. An apparently increased local concentration and transit time is detected at regions of local curvature (or pits), since at these sites more membrane area is located in the observation spot compared to flat regions. This effect is a result of the observation mode, where the locally curved membrane topography is projected onto a flat 2D surface[25].

Supplementary References

1 Honigmann, A., Mueller, V., Hell, S. W. & Eggeling, C. STED microscopy detects and quantifies liquid phase separation in lipid membranes using a new far-red emitting fluorescent phosphoglycerolipid analogue. *Faraday Discussion* **161** 77–89 (2013).

2 Spillane, K. M. *et al.* High-Speed Single-Particle Tracking of GM1 in Model Membranes Reveals Anomalous Diffusion due to Interleaflet Coupling and Molecular Pinning. *Nano Lett* **14**, 5390−5397 (2014).

3 Petersen, N. O., Hoddelius, P. L., Wiseman, P. W., Seger, O. & Magnusson, K.-E. Quantification of Membrane Receptor Distributions by Image Correlation Spectroscopy: Concept and Application. *Biophys J* **65**, 1135-1146 (1986).

4 Digman, M. A. *et al.* Fluctuation Correlation Spectroscopy with a Laser-Scanning Microscope: Exploiting the Hidden Time Structure. *Biophys J* **88**, L33–L36 (2005).

5 Hedde, P. N. *et al.* Stimulated emission depletion-based raster image correlation spectroscopy reveals biomolecular dynamics in live cells. *Nature Communications* **4**, 2093 (2013).

6 Eggeling, C. *et al.* Direct observation of the nanoscale dynamics of membrane lipids in a living cell. *Nature* **457**, 1159-U1121 (2009).
7 Ringemann, C. *et al.* Exploring single-molecule dynamics with fluorescence nanoscopy. *New J Phys* **11**, 103054 (2009).
8 Wawrezinieck, L., Rigneault, H., Marguet, D. & Lenne, P. F. Fluorescence correlation spectroscopy diffusion laws to probe the submicron cell membrane organization. *Biophys J* **89**, 4029-4042 (2005).
9 Ruan, Q. Q., Cheng, M. A., Levi, M., Gratton, E. & Mantulin, W. W. Spatial-Temporal Studies of Membrane Dynamics: Scanning Fluorescence Correlation Spectroscopy (SFCS). *Biophys J* **87**, 1260-1267 (2004).
10 Ries, J. & Schwille, P. Studying Slow Membrane Dynamics with Continuous Wave Scanning Fluorescence Correlation Spectroscopy. *Biophys J* **91**, 1915-1924 (2006).